Spring 2014

Neutral Hydrogen Emission in Nearby X-ray-Selected Active Galaxies

Erin George
University of Colorado Boulder

Neutral Hydrogen Emission in Nearby X-ray-Selected Active Galaxies

Erin George
erin.george@colorado.edu

April 2014

Thesis Advisor
Jeremy Darling – APS Department

Defense Committee
Jeremy Darling – APS Department
John Cumalat – Physics Department,
Honors Representative
Steven Pollock – Physics Department

Neutral Hydrogen Emission in Nearby X-ray-Selected Active Galaxies

E. George, J. Darling, L. Winter

Center for Astrophysics and Space Astronomy, University of Colorado at Boulder

593 UCB, Boulder, CO 80309, USA

erin.george@colorado.edu

ABSTRACT

We have searched for neutral hydrogen (H I) in 95 active galaxies using the 100-meter Green Bank Telescope. The sample includes only nearby active galaxies up to 220 Mpc away (redshifts up to 0.05). Our galaxies all contain Seyfert active galactic nuclei (AGN) detected in the hard X-ray (14-195 keV) by the Swift Gamma-ray Burst satellite's Burst Alert Telescope (BAT) 22-month survey. The hard X-ray emission is purely from the AGN with no component from star formation in the host galaxy. By using this band for our selection method we include Seyfert AGN that are otherwise obscured in the optical and ultraviolet spectra. We present the H I systemic velocities, H I integrated line fluxes, and H I masses for the 37 galaxies with H I emission. Using published optical data we present maximum rotational velocities and dynamical masses for 27 of the galaxies with emission. We used the X-ray flux from the Swift BAT 22-month survey to calculate the corresponding X-ray luminosity, which is an estimate of the accretion rate of the AGN. We used this to explore relationships between the accretion rate of the AGN and properties of the host galaxy - mainly the cold gas content and dynamical mass. We present the parameters of the relationships between both cold gas mass and dynamical mass with accretion rate of the AGN.

1. Introduction

We are studying active galactic nuclei (AGN), which are supermassive black holes (SMBHs) that are accreting gas and dust in the centers of their host galaxies. The goal of this project is to explore potential relationships between the host galaxy and its SMBH. Specifically we are searching for either a correlation or lack of correlation between the accretion rate of the SMBH and the cold gas and dark matter mass content of the host galaxy. To

do this, we have a sample of 95 galaxies at redshifts up to 0.05 that were selected from the Swift Gamma Ray Burst satellite's Burst Alert Telescope (BAT) 22-month survey. From this survey, we have the 14-195 keV hard X-ray emission from the accretion disk of each SMBH. We independently observed the neutral hydrogen content of the host galaxy for each of these AGN using the Green Bank Telescope (GBT). This data set combined with published optical data give us the cold gas content of the galaxy and dynamical mass, and thus an estimate of the dark matter mass. We will use the published Swift data as well as the neutral hydrogen data from our own observations for our investigation of relationships between the AGN and its host.

Following the convention of papers in the Astronomy field, I am using 'we' instead of 'I' for the work that was completed. I have written all of this paper, completed most of the observations, all of the reductions, and all of the analysis. Dr. Darling advised me on this project. Dr. Winter selected the galaxies in the survey, applied for the telescope time, helped with two of the long observing sessions, and completed the baseline subtraction step.

1.1. Seyfert AGN

Before we delve into the depths of the project, we must first understand what AGN are and what characteristics they exhibit. An AGN is an accreting SMBH in the center of a galaxy. The AGN has a small angular size, meaning the accretion disk and SMBH are located in the sub-parsec region of the galaxy, which itself is on the scale of kiloparsecs. The AGN has a high luminosity comparable to that of the host galaxy, usually between 1% and 10,000% of the galaxy's luminosity. AGN exhibit a broad-band continuum from the infrared spectrum to the soft X-ray region that falls off at higher frequencies. Those with relativistic jets have continua that extend into the radio spectrum. They have strong, broad emission lines compared to the widths of stellar absorption features. There are numerous classifications of AGN, but our survey consists solely of Seyfert galaxies.

Seyfert galaxies contain low-luminosity AGN. Although the AGN is still highly luminous, its luminosity is low enough that the host galaxy can be observed. Seyfert AGN are usually found in spiral galaxies (Heckman 1978). They are commonly divided into two categories - type 1 and type 2. Seyfert 1 AGN have narrow permitted and forbidden emission lines with widths of hundreds of km s^{-1}, as well as broad permitted lines with higher widths up to ten thousand km s^{-1}. Seyfert 2 AGN only have the narrow lines in their spectra. Addi-

tionally, Seyfert 2's have weaker broad-band continuum emission, which makes it difficult to distinguish between the AGN and the stellar content of the galaxy. Hard X-ray photons are high enough in energy to penetrate the gas and dust in the galaxy, allowing us to observe Seyfert 2 AGN in a more unbiased manner without the possibility of missing a detection in the optical spectrum. There are other sub-categories of Seyfert types, 1.2, 1.5, 1.8, and 1.9, which are distinguished using the optical properties of the galaxies. By increasing number, less of the broad emission lines can be seen.

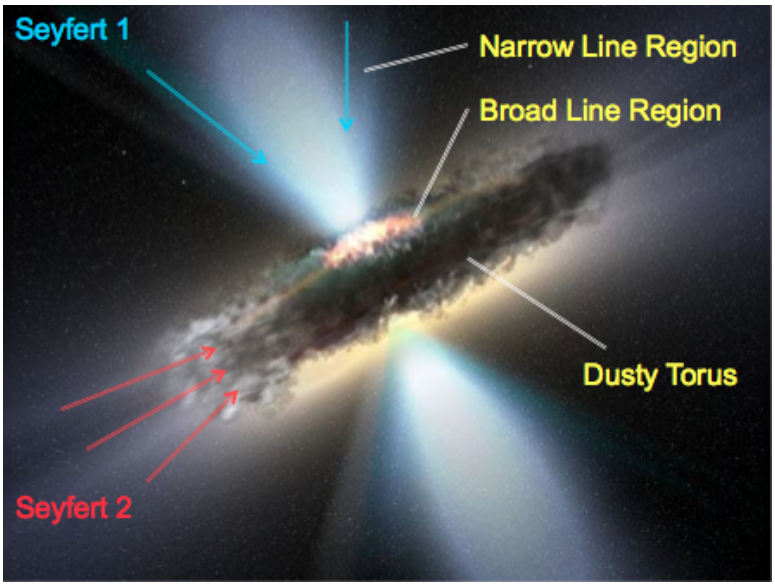

Fig. 1.— Seyfert Viewing Angle: Seyfert 1's are seen through both the Narrow Line Region and the Broad Line Region. Seyfert 2's are seen through the dusty torus, which blocks optical and infrared emission from the Broad Line Region. (Image from http://www.dailygalaxy.com/photos/uncategorized/2007/07/30/supermassive_black_holejpg_1_2.jpg)

The origin of the physical differences between Seyfert 1 and Seyfert 2 galaxies is unknown, but the accepted explanation is that they contain the same physical properties, but we observe different phenomena based on our viewing angle of the AGN (see Figure 1). The Broad Line Region (BLR) contains fast moving gas that surrounds the accretion disk, but is not a part of it. The accretion disk emission stimulates the BLR gas to emit lines in the optical spectrum. The absence of broad forbidden lines from this region indicates the BLR has a higher density. The forbidden transitions are suppressed by collisions because each atom is more likely to collide with another before enough time has passed for the forbidden transitions to take place. The Narrow Line Region (NLR) surrounds a much larger area of the accretion disk. The gas in the NLR is moving more slowly than the gas in the BLR, so the NLR emission lines are not Doppler broadened. Surrounding the SMBH and its accretion

disk is a large dusty torus that absorbs optical and ultraviolet light from the accretion disk and, in the case of Seyfert 2's, emission lines from the BLR.

1.2. Neutral Hydrogen Emission

We observed neutral hydrogen (H I) in our sample. H I emission is the ground state hyperfine spin-flip transition when the electron in the electron-proton pair of hydrogen flips its spin from parallel to anti-parallel with respect to the spin of the nucleus. This transition has an energy of 5.9 μeV, which yields a photon of 1.4204 GHz or 21.105 cm. This transition is forbidden, meaning it will not happen via electric dipole transitions or other easy transition routes and therefore has a low probability of occurring. Consequently, the parallel state has a very long lifetime, making it highly unlikely to be observed on Earth. This transition has a rate of 2.9×10^{-15} s^{-1}, so the galactic scale is large and old enough for us to observe this phenomenon. Neutral hydrogen is spread throughout the disk of the galaxy. The light from H I emission penetrates the dust, unlike some stellar emission, giving us a map of the cold gas in the disk of the galaxy. We can measure the width of the galaxy, the systemic velocity, and cold gas mass of the host, as well as estimate the rotational velocity and dark matter mass of the host using the H I profile.

1.3. Motivation and Outline

Relationships between properties of active galaxies and their SMBHs are not as fully studied as relationships in inactive galaxies and their SMBHs. Masses of SMBHs in active galaxies have been found to be related to rotational velocities of the host galaxies (Ho et al. 2008b). An even stronger relation found by Ho et al. (2008b) is the correlation between SMBH mass and dynamical mass of the host. As far as accretion is concerned, Ho et al. (2003) found no relationship between the optical AGN activity (optical accretion from Hα luminosity) and the global gas content of the host galaxy. Esquej et al. (2014) and Diamond-Stanic & Rieke (2012) found a correlation between AGN accretion and nuclear star formation, which is local star formation near the AGN, not global star formation of the galaxy. This indicates a connection between the AGN and the gas content in sub-kpc region (and even more so in the sub-pc region) around the AGN and its SMBH. Since correlations to the accretion have been found only at small radii, we expect to find no relationship between the accretion rate of the SMBH and the global cold gas and dark matter mass contents. In this study, we search for evidence to support our prediction.

We present our work as follows. Section 2 describes the Swift BAT 22-month survey and its significance, as well as observations and data reduction techniques for our H I data. Section 3 presents the H I observation results, detection statistics, measured quantities, and derived quantities. Section 4 presents the correlations between the accretion rate of the SMBH and both the dark matter mass of the host and the cold gas mass of the host, as well as the respective statistics of the correlations, a comparison between H I and optical systemic velocities, and a comparison to the literature of our measurements and correlations. In Section 5, we discuss the implications of the correlations we found in Section 4. Section 6 summarizes our main conclusions.

2. Observations and Data Reductions

2.1. X-ray

The sample was selected from the Seyfert galaxies in the Swift BAT 22-month survey. These AGN were detected and observed using the BAT instrument on the Swift satellite. During down time between gamma ray bursts, the BAT goes into "survey" mode where it observes levels of radiation that exceed the threshold set by the background measurements. The reductions and analysis were completed by Tueller et al. (2010). The hard X-ray band the BAT observes is radiation directly from the accretion disk around the SMBH. Star formation properties, which usually come from the ultraviolet and far infrared regions of the spectrum, do not have any component from the hard X-ray band. This means the hard X-ray emission is generated by the AGN. Unlike the soft X-ray band, hard X-ray photons penetrate the gas and dust in the galaxy, giving us a concrete way to detect Seyfert 2 AGN that are otherwise obscured in the optical and ultraviolet bands. This gives us a less biased sample because we are able to include these obscured AGN. We can use the X-ray flux and the distance of the galaxy to compute an X-ray luminosity, which is proportional to the accretion rate of the SMBH. Therefore, we have an estimate of the accretion rate from the X-ray luminosity (see Table 3 for the gathered X-ray data).

2.2. H I

For our observations, we used the Green Bank Telescope (GBT) located in Green Bank, West Virginia. The GBT is a 100-m single dish radio telescope with a frequency range of 100 MHz to 100 GHz. It covers roughly 85 percent of the sky with a declination lower limit of $-45°$. The GBT has a 5 arcsecond pointing accuracy. Our sample spans the whole right

ascension range and has a declination range of $-38°$ to $0°$ and $+38°$ to $+81°$. The range of $0°$ to $+38°$ will be covered by the Arecibo H I survey called ALFALFA. Our observation sessions were from April 20th, 2012 to June 17th, 2012 (see Table 1 for observation details). For each galaxy, we completed two 10-minute OffOn scans, where 5 minutes were spent off the source to measure the background continuum and account for instrumental effects, then 5 minutes on the source to include the source's radiation. Two linear polarizations were measured for each of the two scan pairs over a 50 MHz bandwidth over 4095 channels (12 km s^{-1} channel width), with 100 integrations per scan pair (6s records). Two of the sources, Mrk6 and NGC5505 were observed for additional time because they showed strong absorption features from the initial observations (see Section 3.2). The spectral reductions were done using GBTIDL procedures. The off scans were subtracted from the on scans and then normalized using the sky spectrum. The two scan pairs and both of their polarizations were averaged, and the resulting spectrum was Hanning smoothed. A baseline was fit to each source and then subtracted by Dr. Lisa Winter. The resulting final spectra had velocity resolutions of 10 km s^{-1} (see Figure 3 for spectra). We typically found rms noise levels of 7-27 mJy per channel.

In some cases, spectra contained large radio frequency interference (RFI) features. Most RFI did not interfere strongly with the location of the emission. Some, however, had RFI at the same frequency where we expected the detections. For the 11 galaxies with RFI on or near where the detection would be, we used a routine written by Ting Yan to smooth the spectrum and reduce the RFI. This routine took the median of the spectra in each polarization of each scan, and then averaged those medians together to create the final spectrum. This routine was used more to identify the presence of any emissions, rather than to seek a final spectrum for analysis. Unfortunately, no presence of emission or absorption were seen for these 11 galaxies. Additionally, 6 of the sources had standing wave interference caused by resonances in the telescope from the Sun. The observations took place during a solar maximum year, and due to their position in the sky with respect to the Sun, the spectra contained 8-10 MHz (30-37.5 m) standing waves. This is most likely due to aperture blockage from the orientation of the telescope with respect to the Sun. For these 6 galaxies, we were unable to clearly determine the presence of neutral hydrogen emission or absorption.

Table 1. Journal of Observations

Session Number (1)	Date (2)	Number of Hours (3)	Number of Targets (4)
1	20 April 2012 - 21 April 2012	9.5	22
2	26 April 2012	4	9
3	22 May 2012 - 23 May 2012	11.5	27
4	24 May 2012	9	23
5	4 June 2012 - 5 June 2012	3	5 (*)
6	5 June 2012	1	2 (**)
7	15 June 2012	2	4
8	17 June 2012	1.5	5

Note. — (1) Observation Session Number, from program AGBT12A-253. (2) Data of observation, often spans the night between two dates. (3) Number of hours of observation session. (4) Number of targets observed in session. (*) This session included additional time for Mrk6. (**) This session included additional time for NGC5506.

3. Results and Measurements

3.1. H I Detections

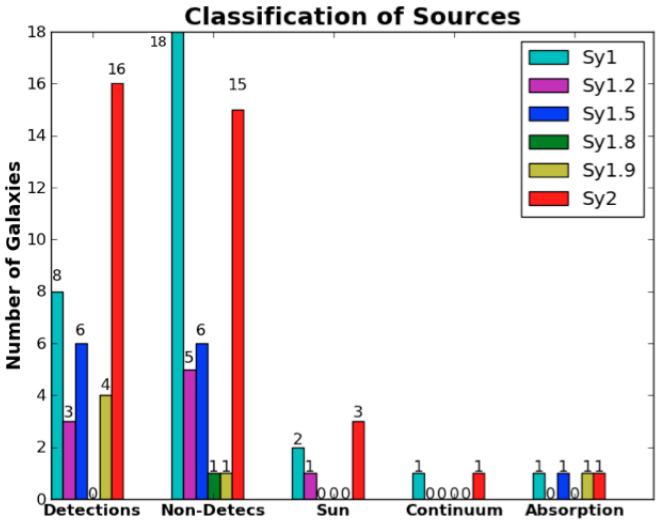

Fig. 2.— Summary of the results of our neutral hydrogen observations, separated by Seyfert types. The first group shows the objects with H I emission, the second group shows objects with no H I emission or absorption, the third group shows the objects with solar interference, the fourth group shows the two objects with strong continua but no H I emission or absorption features, and the fifth group shows the four objects with significant absorption features.

Out of the 95 galaxies in our study, 41 had H I detections (see Figure 2). Of these detections, 4 had significant absorption features. As mentioned previously, 6 galaxies remain unclassified as they had significant solar interference. Two of the sources had large radio continuum features, but no H I emission or absorption. The results of the survey can be seen in Table 2. If we group Seyfert 1, 1.2, and 1.5 galaxies into type I and Seyfert 1.8, 1.9, and 2 galaxies into type II, we have clearer detection rates for the different Seyfert types. For type I, we found 17 out of 52 galaxies had emissions, giving us an emission detection rate of 33%. For type II, we found 20 out of the 43 galaxies had emissions, which is an emission detection rate of 54%. The higher detection rate for type II could indicate that, on average, Seyfert type II galaxies have a larger cold gas reservoir.

Table 2. The Sample

Object Name (1)	α (2)	δ (3)	v_{sys} (4)	Seyfert Type (5)	H I Profile (6)
2MASXJ00253292+6821442	00:25:17.2	+68:21:04.1	3597	Sy2	Emission
NGC235A	00:42:49.3	-23:29:28.4	6664	Sy1	None
MCG-01-05-047	01:52:47.5	-03:27:44.6	5156	Sy2	Emission
NGC788	02:01:03.2	-06:48:42.4	4077	Sy2	None
Mrk1018	02:06:15.3	-00:18:25.6	12723	Sy1.5	None
LEDA138501	02:09:34.6	+52:26:47.0	14749	Sy1	None
NGC985	02:34:39.0	-08:45:35.0	12891	Sy1	None
NGC1052	02:41:19.5	-08:14:41.4	1510	Sy2	Emission
NGC1068	02:42:50.4	-00:01:59.4	1136	Sy2	Emission
[HB89]0241+622	02:45:06.1	+62:27:01.5	13190	Sy1	None
2MFGC02280	02:50:49.1	+54:41:13.4	4541	Sy2	Emission
MCG-02-08-014	02:52:42.3	-08:28:50.7	5021	Sy2	None
NGC1142	02:55:11.6	-00:11:48.7	8649	Sy2	None
ESO417-G006	02:56:23.0	-32:12:41.8	4883	Sy2	None
NGC1194	03:04:02.6	-01:07:29.8	4077	Sy1	Emission
NGC1275	03:19:48.1	+41:31:09.3	5264	Sy2	Continuum
UGC02724	03:24:45.8	+40:44:41.8	14309	Sy2	Sun
ESO482-14	03:36:43.0	-25:10:48.6	13103	Sy2	None
ESO548-G081	03:42:02.0	-21:14:40.9	4340	Sy1	None
ESO549-G049	04:02:24.9	-18:08:14.5	7881	Sy2	Sun
IRAS04124-0803	04:14:47.4	-07:54:50.8	11365	Sy1	Sun
3C111.0	04:18:19.7	+38:02:18.4	14539	Sy1	Continuum
MCG-02-12-050	04:38:12.6	-10:48:24.8	10897	Sy1.2	Sun
1RXSJ045205.0+493248	04:51:56.4	+49:30:30.2	8693	Sy1	None
2MASXJ05054575-2351139	05:05:46.8	-23:50:40.2	10504	Sy2	None
Ark120	05:16:10.7	-00:09:33.0	9683	Sy1	Sun
ESO362-18	05:19:23.8	-32:41:11.1	3732	Sy1.5	Emission
IRAS05218-1212	05:24:17.4	-12:14:56.4	14689	Sy1	Emission
MCG-05-14-012	05:43:42.1	-27:41:13.9	2973	Sy1.2	Emission
NGC2110	05:52:09.6	-07:27:21.2	2335	Sy2	Emission
MCG+08-11-011	05:54:55.0	+46:25:21.2	6139	Sy1.5	Emission
EXO0556.3-3820	05:58:02.0	-38:20:04.7	10154	Sy1	None
Mrk3	06:15:39.2	+71:02:09.9	4050	Sy2	Emission
ESO426-G002	06:23:50.7	-32:14:56.0	6724	Sy2	Emission
ESO490-IG026	06:40:10.5	-25:53:58.6	7434	Sy1.2	None
Mrk6	06:52:22.0	+74:26:01.7	5639	Sy1.5	Absorption

Table 2—Continued

Object Name (1)	α (2)	δ (3)	v_{sys} (4)	Seyfert Type (5)	H I Profile (6)
UGC03601	06:55:57.8	+39:59:34.4	5132	Sy1.5	None
Mrk79	07:42:25.7	+49:49:34.2	6652	Sy1.2	Emission
MRK10	07:47:33.4	+60:57:39.8	8771	Sy1.2	Emission
FAIRALL0272	08:23:04.7	-04:53:38.4	6541	Sy2	Emission
2MASXJ09043699+5536025	09:04:18.3	+55:35:17.9	11092	Sy1	None
2MASXJ09112999+4528060	09:11:24.3	+45:33:24.2	8028	Sy2	Sun
MCG-01-24-012	09:20:47.6	-08:06:10.3	5887	Sy2	Emission
2MASXJ09235371-3141305	09:23:48.4	-31:42:56.2	12666	Sy1.9	None
Mrk110	09:25:09.0	+52:17:49.3	10579	Sy1	None
NGC2992	09:45:45.7	-14:18:58.7	2311	Sy2	Emission
MCG-05-23-016	09:47:39.6	-30:56:42.7	2545	Sy2	None
NGC3081	09:59:30.8	-22:49:57.3	2386	Sy2	Emission
NGC3079	10:01:52.2	+55:38:55.7	1115	Sy2	Emission
NGC3281	10:31:48.2	-34:51:51.0	3198	Sy2	Absorption
NGC3516	11:06:35.6	+72:34:23.8	2650	Sy1.5	None
UGC06527	11:32:55.2	+52:57:54.9	8346	Sy2	None
NGC3718	11:32:55.2	+52:57:54.9	992	Sy1	Emission
UGC06728	11:44:15.9	+79:40:46.5	1954	Sy1.2	None
2MASXJ11454045-1827149	11:45:38.8	-18:25:22.9	9878	Sy1	None
NGC3998	11:57:40.1	+55:28:23.1	1040	Sy1	Emission
NGC4051	12:03:12.3	+44:31:24.4	698	Sy1.5	Emission
MRK0198	12:09:20.9	+47:01:09.6	7260	Sy2	Emission
NGC4138	12:09:26.1	+43:40:52.6	887	Sy1.9	Emission
NGC4151	12:10:32.7	+39:24:21.3	995	Sy1.5	Emission
M106	12:19:30.3	+47:20:46.6	446	Sy1.9	Emission
ESO506-G027	12:38:55.7	-27:18:45.7	7500	Sy2	None
LEDA170194	12:39:08.4	-16:12:21.9	10993	Sy2	None
NGC4593	12:39:37.0	-05:20:58.1	2698	Sy1	Emission
SBS1301+540	13:04:07.6	+53:46:17.9	8957	Sy1	Absorption
MCG-03-34-064	13:22:29.6	-16:43:24.1	4958	Sy1.8	None
MCG-06-30-015	13:35:53.5	-34:17:50.4	2323	Sy1.2	None
IC4329A	13:49:19.1	-30:18:42.0	4811	Sy1.2	None
Mrk279	13:53:04.1	+69:18:49.6	9128	Sy1.5	None
NGC5506	14:13:14.0	-03:12:40.6	1852	Sy1.9	Absorption
ESO511-G030	14:19:18.5	-26:38:42.3	6712	Sy1	Emission
MRK0817	14:36:18.8	+58:46:21.3	9428	Sy1.5	None

Table 2—Continued

Object Name (1)	α (2)	δ (3)	v_{sys} (4)	Seyfert Type (5)	H I Profile (6)
NGC5728	14:42:25.7	-17:14:20.7	2788	Sy2	Emission
NGC5899	15:15:01.2	+42:04:33.1	2563	Sy2	Emission
MCG-01-40-001	15:33:11.6	-08:37:42.9	6808	Sy2	None
Mrk290	15:35:55.9	+57:51:11.2	8867	Sy1	None
2MASXJ15462424+6929102	15:46:24.3	+69:27:38.6	11392	Sy2	None
NGC5995	15:48:25.3	-13:44:06.2	7551	Sy2	Emission
CGCG367-009	16:20:21.6	+81:02:22.7	8214	Sy2	None
2MASXJ16481523-3035037	16:48:11.6	-30:35:37.0	9293	Sy1	None
ARP102B	17:19:48.1	+48:58:15.2	7245	Sy1	Emission
AXJ1737.4-2907	17:37:31.6	-29:09:05.7	6415	Sy1	None
2MASSJ17485512-3254521	17:48:55.5	-32:57:53.8	5995	Sy1	None
NGC6814	19:42:37.8	-10:20:56.9	1561	Sy1.5	Emission
2MASXJ20183871+4041003	20:18:32.7	+40:42:50.1	4317	Sy2	None
Mrk509	20:44:14.7	-10:44:03.4	10312	Sy1.2	None
4C50.55	21:24:39.7	+50:58:26.0	5995	Sy1	None
SWIFTJ212745.58+565635.6	21:27:43.4	+56:57:52.1	4406	Sy1	None
6dFJ2132022-334254	21:31:59.0	-33:45:46.3	8780	Sy1	None
2MASXJ21355399+4728217	21:36:11.3	+47:30:23.7	7494	Sy1	None
NGC7172	22:02:03.2	-31:52:41.7	2602	Sy2	None
NGC7314	22:35:40.7	-26:05:33.6	1427	Sy1.9	Emission
MRK0915	22:36:40.6	-12:33:28.5	7227	Sy1	Emission
UGC12282	22:58:51.8	+40:54:40.2	5093	Sy1.9	Emission
Mrk926	23:04:41.6	-08:40:30.3	14048	Sy1.5	None

Note. — (1) Object Name. (2) Right Ascension (J2000.0). (3) Declination (J2000.0). (4) Optical Systemic Velocity (km/s). (5) Seyfert Classification (1, 1.2, 1.5, 1.8, 1.9, or 2). (6) Result of H I Observations. 'Emission' corresponds to an emission profile seen centered around the systemic velocity, where as 'None' corresponds to no H I flux profile observed. 'Absorption' are sources with significant features that extend below zero flux. 'Sun' are sources that are so far undetermined due to solar interference. 'Continuum' indicates a source with a strong continuum.

Fig. 3.— H I Emission Profiles: H I Flux (Jy) vs. Velocity (km/s).

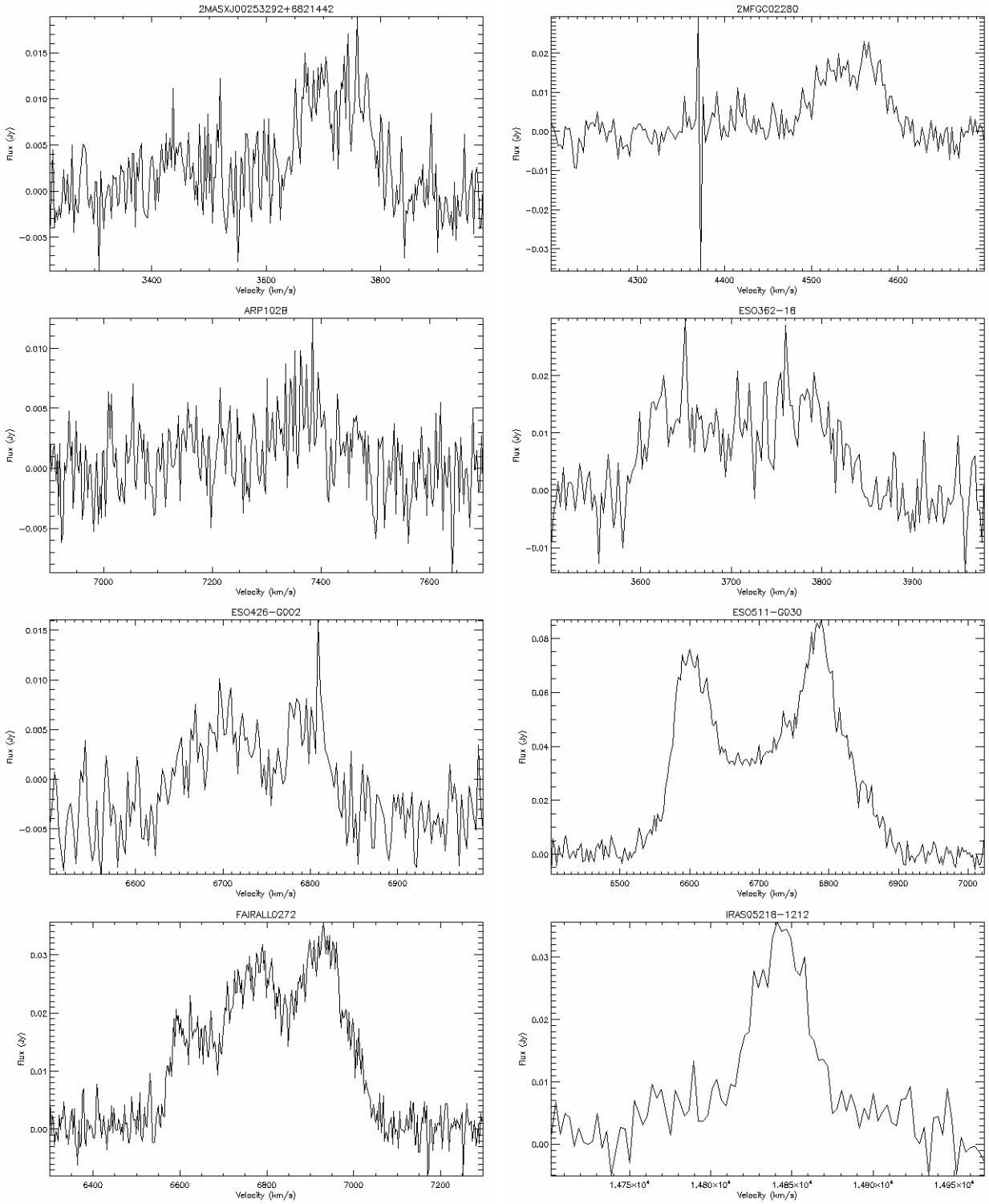

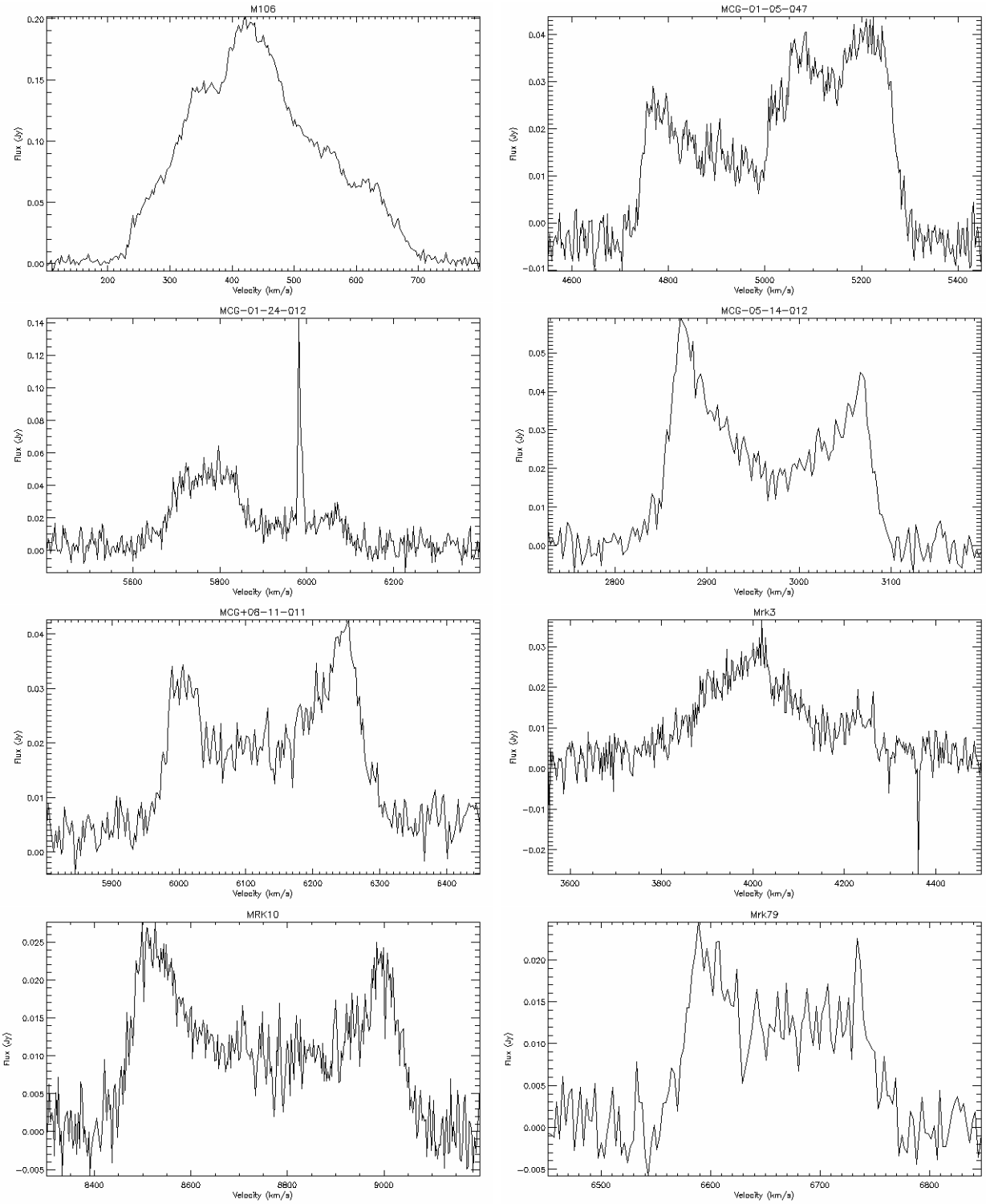
M106
MCG−01−05−047
MCG−01−24−012
MCG−05−14−012
MCG+08−11−011
Mrk3
MRK10
Mrk79
Flux (Jy)
Velocity (km/s)

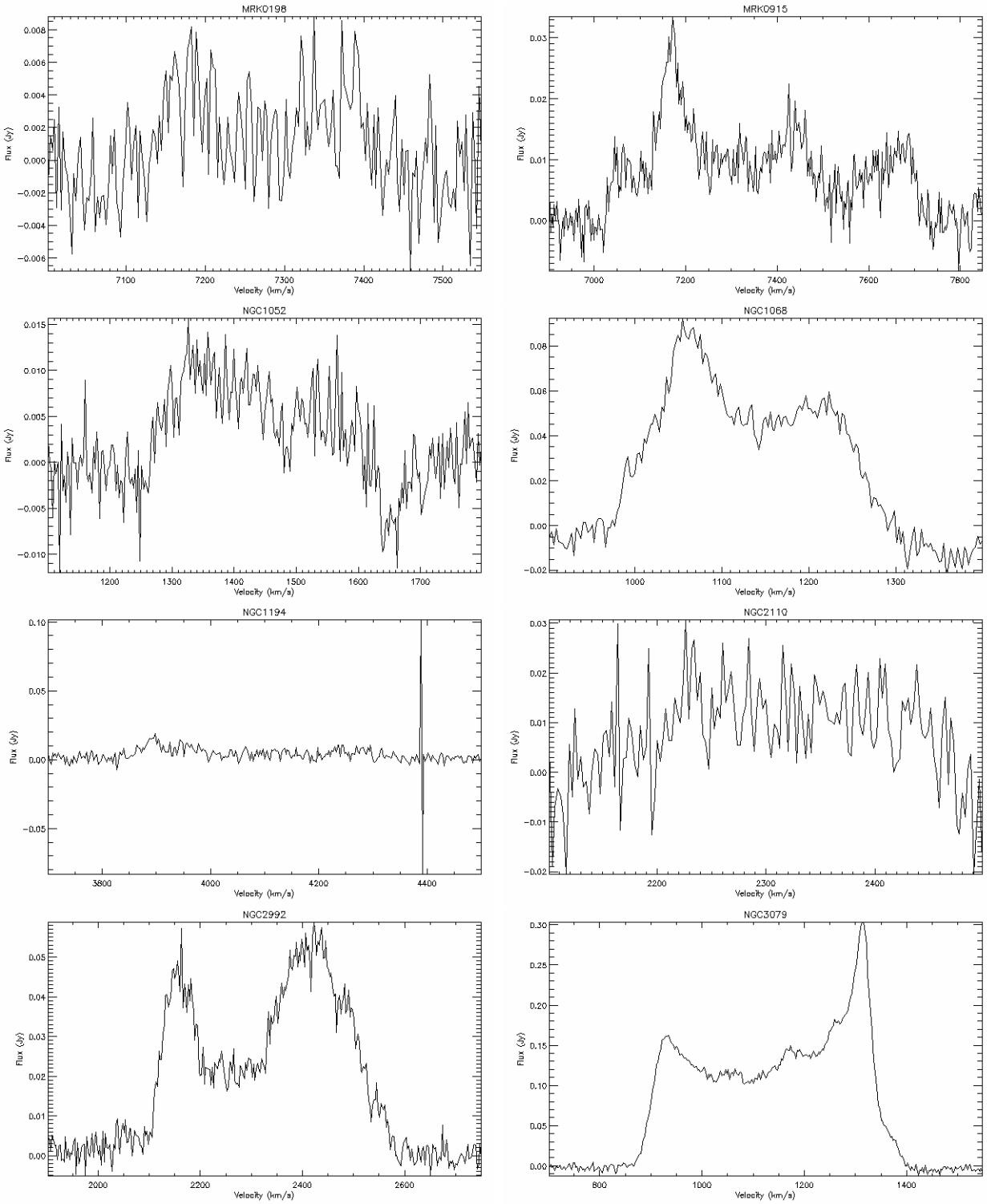
MRK0198
Flux (Jy)
Velocity (km/s)
MRK0915
Flux (Jy)
Velocity (km/s)
NGC1052
Flux (Jy)
Velocity (km/s)
NGC1068
Flux (Jy)
Velocity (km/s)
NGC1194
Flux (Jy)
Velocity (km/s)
NGC2110
Flux (Jy)
Velocity (km/s)
NGC2992
Flux (Jy)
Velocity (km/s)
NGC3079
Flux (Jy)
Velocity (km/s)

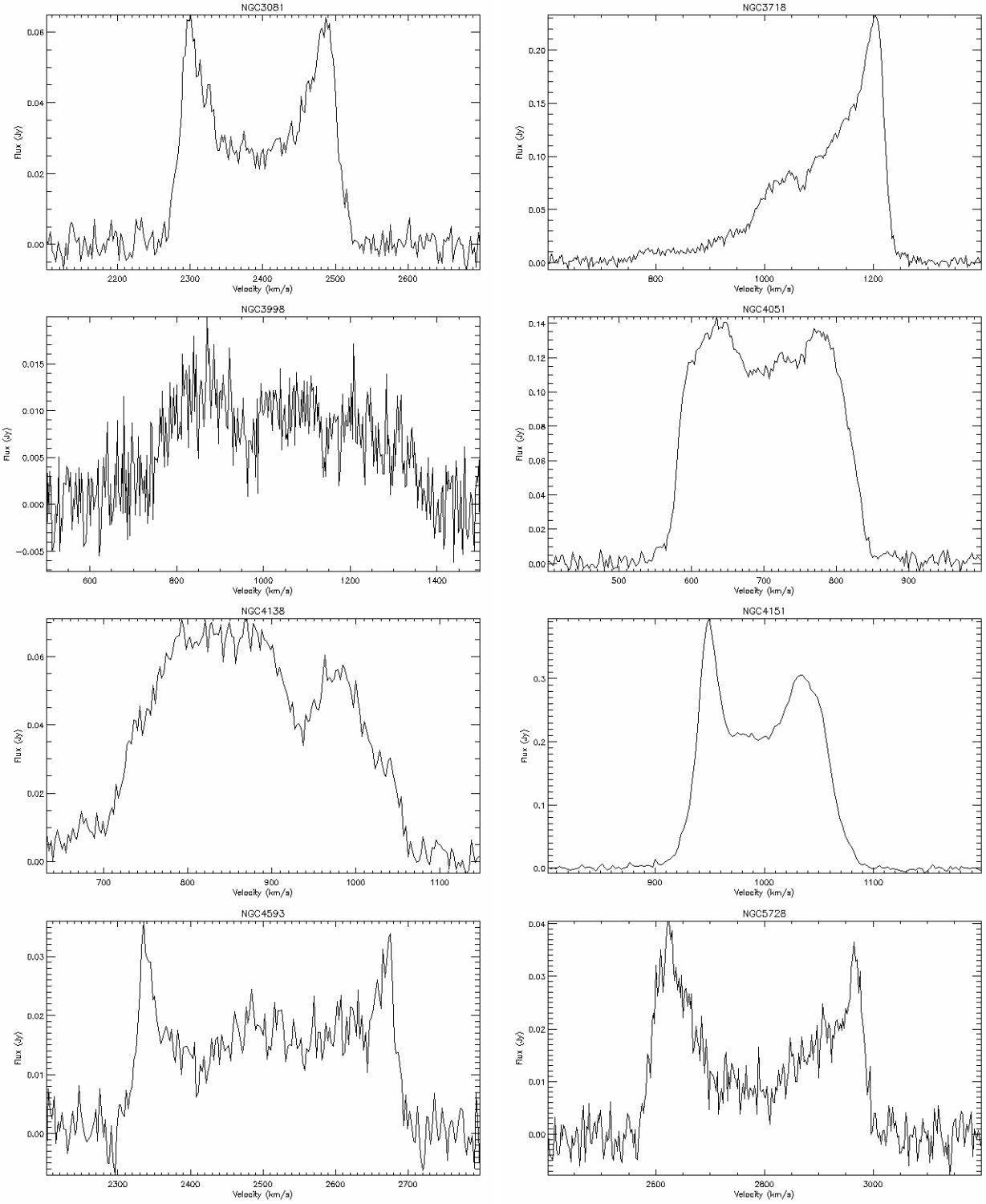
NGC3081
NGC3718
NGC3998
NGC4051
NGC4138
NGC4151
NGC4593
NGC5728
Flux (Jy)
Velocity (km/s)

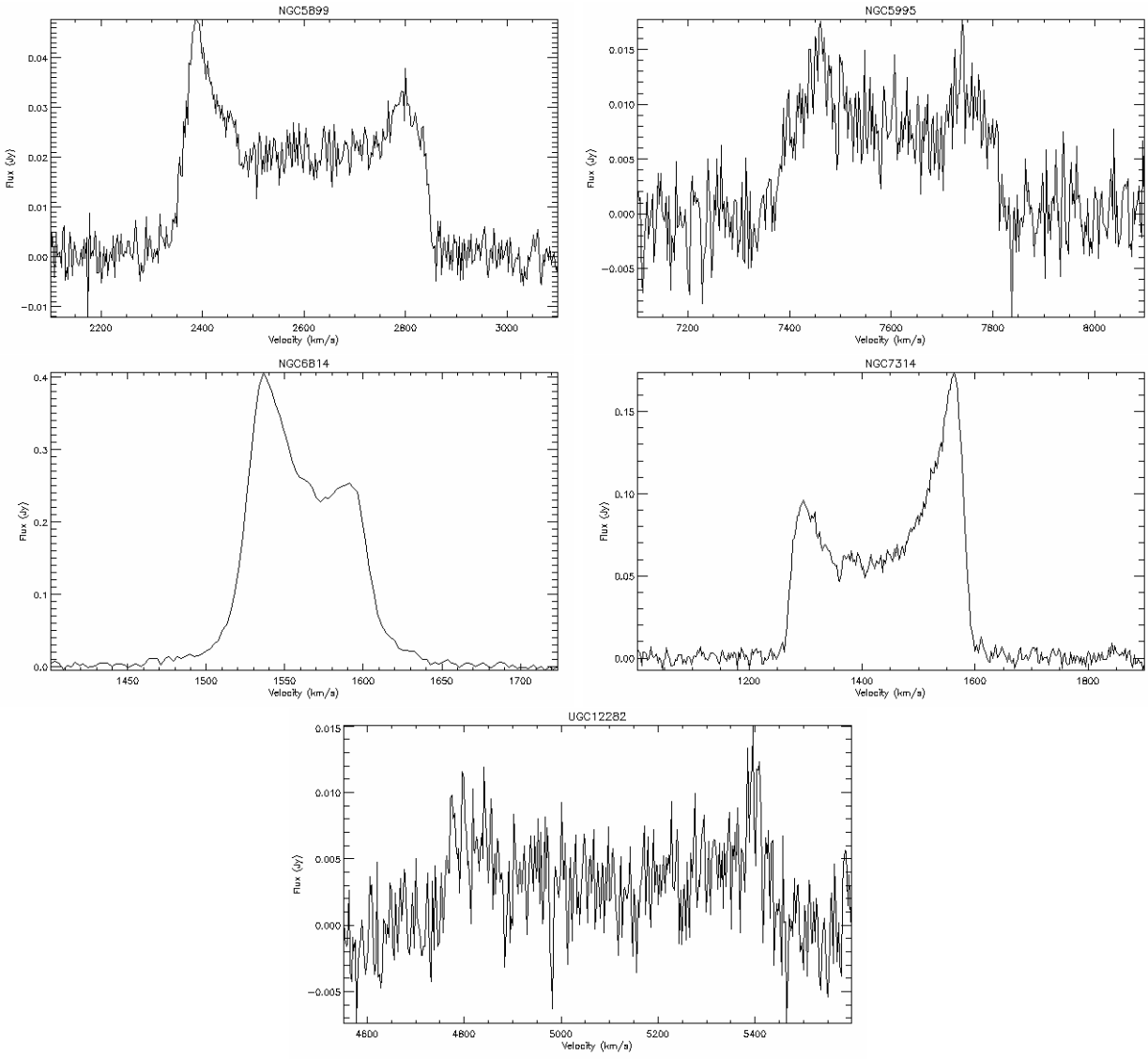
NGC5899
Flux (Jy)
Velocity (km/s)
NGC5995
Flux (Jy)
Velocity (km/s)
NGC6814
Flux (Jy)
Velocity (km/s)
NGC7314
Flux (Jy)
Velocity (km/s)
UGC12282
Flux (Jy)
Velocity (km/s)

3.2. H I Aborption Profiles

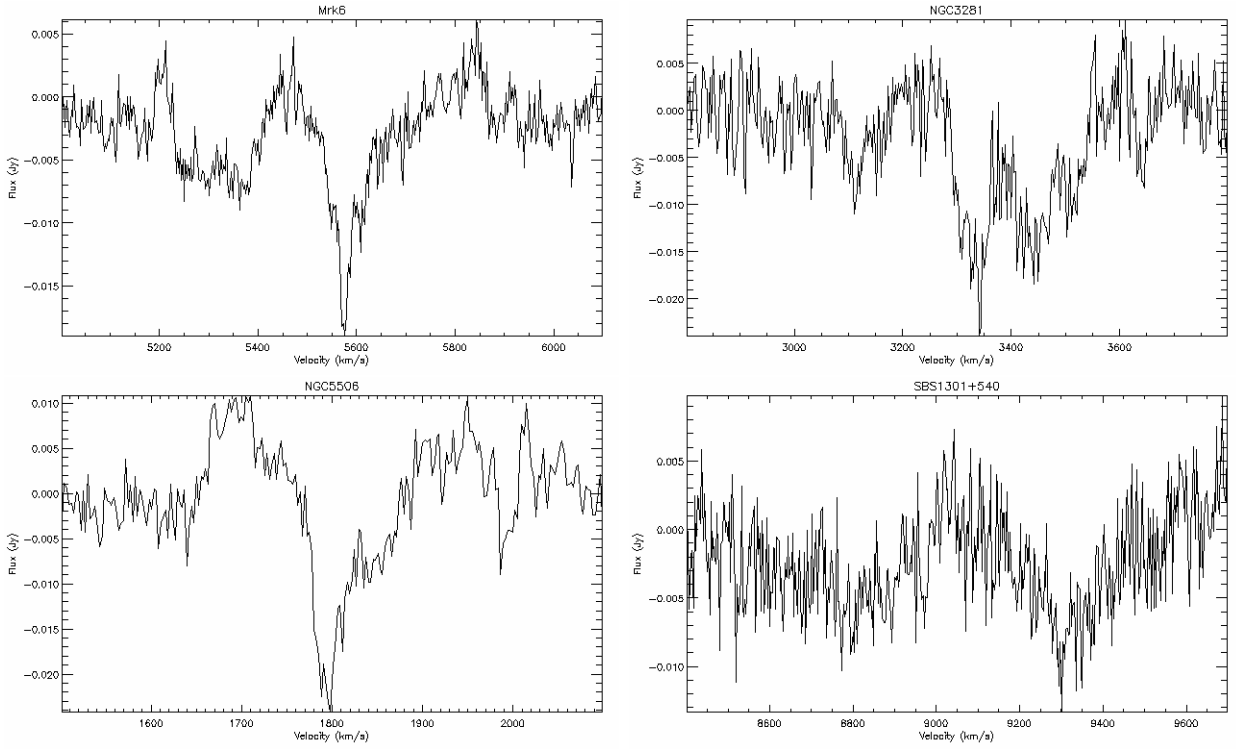

Fig. 4.— H I Absorption Profiles

From our sample, we found four sources with significant absorption features that did not also have significant emission features (see Figure 4). Though this study does not analyze these sources, they will be covered in the accompanying paper by Dr. Lisa Winter (in prep). It should be noted that this is a higher rate of absorption-only detections (not detections with significant absorption and emission features) than found in Ho et al. (2008). Their sample was mainly type I Seyferts. For our four objects with significant absorption features, the Seyfert types covered the whole range (1, 1.5, 1.9, and 2.0). We were able to include galaxies with obscured AGN, which has allowed us to find more sources with absorption than studies that have only type I Seyferts.

Table 3. Compiled Data for H I Emission Objects

Object Name (1)	i (deg) (2)	D_L (Mpc) (3)	D_{25} (arcmin) (4)	X-ray Flux(Error) (10^{-11} erg s^{-1} cm^{-2}) (5)	X-ray Luminosity(Error) (10^{42} erg s^{-1}) (6)
2MASXJ00253292+6821442	...	51.2	...	3.02(0.66)	9.47(2.20)
2MFGC02280	...	64.8	...	3.30(0.57)	16.6(3.04)
ARP102B	40.0	104.0	0.95	1.89(0.45)	24.5(5.90)
ESO362-18	52.8	52.1	1.08	6.22(0.52)	20.2(2.29)
ESO426-G002	22.7	95.4	1.19	2.72(0.45)	29.6(5.06)
ESO511-G030	47.6	96.2	1.40	4.71(0.65)	52.2(7.52)
FAIRALL0272	...	95.4	...	4.02(0.71)	43.8(7.05)
IRAS05218-1212	...	214.8	...	2.50(0.54)	138(29.9)
M106	74.9	9.0	2.27	2.80(0.63)	0.270(0.135)
MCG+08-11-011	47.6	87.9	1.32	9.64(0.61)	89.1(6.95)
MCG-01-05-047	90.0	72.2	1.46	2.78(0.46)	17.3(3.03)
MCG-01-24-012	...	84.2	1.13	4.58(0.51)	38.9(4.70)
MCG-05-14-012	45.8	42.2	...	2.05(0.44)	4.37(1.02)
MRK0198	0.0	104.0	0.90	2.15(0.42)	27.8(5.54)
MRK0915	79.1	103.7	0.99	4.99(0.71)	64.2(9.47)
MRK10	72.0	126.4	1.25	3.12(0.54)	59.6(10.5)
Mrk3	31.1	55.9	1.26	15.70(0.61)	58.7(4.78)
Mrk79	0.0	94.3	1.08	4.89(0.52)	52.0(5.96)
NGC1052	49.4	17.8	1.48	3.75(0.67)	1.42(0.408)
NGC1068	33.5	12.5	1.85	3.72(0.53)	0.695(0.244)
NGC1194	60.3	53.7	1.25	3.64(0.60)	12.6(2.27)
NGC2110	...	33.1	1.23	35.00(0.70)	45.9(5.62)
NGC2992	85.3	30.5	1.55	4.82(0.63)	5.36(0.993)
NGC3079	90.0	17.6	1.90	3.44(0.44)	1.27(0.333)
NGC3081	41.0	32.5	1.32	10.20(0.67)	12.9(1.80)
NGC3718	66.0	16.2	1.91	2.69(...)	0.845(0.209)
NGC3998	35.8	16.6	1.43	3.03(0.48)	0.999(0.288)
NGC4051	44.8	12.7	1.72	4.34(0.35)	0.838(0.272)
NGC4138	52.0	15.3	1.41	3.69(0.45)	1.03(0.298)
NGC4151	47.6	17.1	1.80	62.20(0.46)	21.8(5.09)
NGC4593	44.8	44.0	1.59	9.79(0.62)	22.7(2.51)
NGC5728	59.5	29.1	1.49	10.50(0.71)	10.6(1.63)
NGC5899	76.9	36.8	1.50	2.15(0.42)	3.48(0.779)
NGC5995	...	108.5	...	4.51(0.61)	63.5(8.91)
NGC6814	22.7	22.8	1.48	7.82(0.69)	4.86(0.955)
NGC7314	68.6	19.0	1.66	4.63(0.59)	2.00(0.492)
UGC12282	90.0	72.7	1.28	2.49(0.50)	15.7(3.28)

Note. — The notation '...' means the information is unknown. (1) Object Name. (2) Inclination in degrees, found using Equation 2, where q (the ratio of minor to major axes) was found in NED. (3) Luminosity distance. This value is found in Koss et al. (2011), with supplemental distances from NED where needed. The uncertainties were not listed but assumed to be 2 Mpc. (4) Optical diameter measured in de Vaucouleurs et al. (1991). Uncertainty assumed to be 0.1 arcmin. (5) X-ray flux and error in erg s^{-1} cm^{-2} from Swift BAT 22-month survey. (6) X-ray luminosity and error in erg s^{-1} calculated from the X-ray flux and luminosity distance.

Table 4. H I Properties

Object Name (1)	RMS Noise (Jy) (2)	v_{sys} (Error) (km/s) (3)	W_{20} (Error) (km/s) (4)	Integrated H I Flux (Error) (Jy km/s) (5)	v_m (Error) (km/s) (6)	M_{HI} (Error) (10^9 $M_\odot$) (7)	M_{dyn} (Error) (10^{10} $M_\odot$) (8)
2MASXJ00253292+6821442	0.0098	3597.0(15.8)	469.7(31.6)	3.5(1.6)	...(...)	2.16(1.01)	...(...)
2MFGC02280	0.0093	4531.7(15.0)	212.3(30.0)	2.3(1.5)	...(...)	2.27(1.52)	...(...)
ARP102B	0.0077	7278.8(12.5)	289.2(24.9)	1.4(1.3)	194.9(18.9)	3.51(3.25)	7.51(1.66)
ESO362-18	0.0151	3712.2(24.5)	245.6(49.0)	3.2(2.5)	132.3(30.4)	2.06(1.61)	1.97(0.923)
ESO426-G002	0.0080	6722.6(12.9)	164.3(25.8)	1.0(1.3)	167.3(32.8)	2.16(2.83)	6.36(2.55)
ESO511-G030	0.0098	6713.4(6.5)	296.2(13.0)	14.9(1.6)	174.7(8.6)	32.6(3.79)	8.22(1.01)
FAIRALL0272	0.0075	6798.1(12.2)	436.5(24.3)	10.1(1.2)	...(...)	21.7(2.82)	...(...)
IRAS05218-1212	0.0117	14840.8(18.9)	158.9(37.8)	2.4(1.9)	...(...)	26.4(21.00)	...(...)
M106	0.0084	452.5(12.6)	405.7(25.2)	45.7(1.4)	193.3(13.0)	0.868(0.388)	1.52(0.274)
MCG+08-11-011	0.0088	6132.3(14.2)	346.1(28.5)	8.2(1.5)	208.2(18.9)	14.9(2.74)	10.1(1.98)
MCG-01-05-047	0.0085	5021.4(13.7)	538.0(27.5)	13.2(1.4)	248.6(13.5)	16.3(1.95)	13.0(1.68)
MCG-01-24-012	0.0175	5880.0(28.3)	474.1(56.7)	13.0(2.9)	...(...)	21.8(4.95)	...(...)
MCG-05-14-012	0.0087	2963.8(4.1)	244.4(8.2)	7.1(1.4)	...(...)	3.00(0.665)	...(...)
MRK0198	0.0077	7277.6(12.4)	283.8(24.8)	1.2(1.3)	...(...)	2.98(3.23)	...(...)
MRK0915	0.0084	7339.2(13.7)	670.7(27.3)	8.2(1.4)	317.1(13.6)	20.7(3.63)	20.7(2.74)
MRK10	0.0081	8753.3(13.2)	611.4(26.3)	8.6(1.3)	295.6(13.4)	32.5(5.17)	27.6(3.35)
Mrk3	0.0116	4024.9(18.8)	582.0(37.6)	9.0(1.9)	524.8(35.9)	6.61(1.49)	38.8(6.18)
Mrk79	0.0077	6661.4(12.4)	204.6(24.8)	2.7(1.3)	...(...)	0.195(0.122)	...(...)
NGC1052	0.0092	1415.0(14.9)	359.0(29.8)	2.6(1.5)	214.4(19.5)	0.195(0.122)	2.42(0.490)
NGC1068	0.0186	1129.5(12.6)	282.9(25.1)	14.5(3.1)	226.3(22.7)	0.535(0.205)	2.37(0.526)
NGC1194	0.0101	4059.8(16.4)	513.5(32.7)	3.8(1.7)	273.3(18.6)	2.57(1.15)	10.0(1.59)
NGC2110	0.0279	2315.4(45.1)	345.3(90.2)	4.8(4.6)	...(...)	1.23(1.20)	...(...)
NGC2992	0.0076	2330.6(6.6)	452.7(13.3)	14.9(1.3)	209.4(6.6)	3.27(0.512)	4.14(0.398)
NGC3079	0.0093	1121.5(1.0)	451.7(2.0)	64.7(1.5)	209.0(1.0)	4.73(1.08)	2.92(0.228)
NGC3081	0.0083	2395.2(5.4)	240.8(10.8)	8.7(1.4)	157.8(8.1)	2.18(0.436)	2.14(0.281)

Table 4—Continued

Object Name (1)	RMS Noise (Jy) (2)	v_{sys} (Error) (km/s) (3)	W_{20} (Error) (km/s) (4)	Integrated H I Flux (Error) (Jy km/s) (5)	v_m (Error) (km/s) (6)	M_{HI} (Error) (10^9 $M_\odot$) (7)	M_{dyn} (Error) (10^{10} $M_\odot$) (8)
NGC3718	0.0092	1107.5(1.1)	246.6(2.2)	28.2(1.5)	116.9(1.2)	1.75(0.442)	0.846(0.071)
NGC3998	0.0108	1038.7(17.4)	628.0(34.8)	5.7(1.8)	507.8(29.6)	0.370(0.146)	12.2(1.82)
NGC4051	0.0093	704.5(2.0)	258.9(4.1)	29.7(1.5)	160.5(2.9)	1.13(0.361)	1.12(0.117)
NGC4138	0.0135	883.1(21.8)	344.7(43.6)	17.4(2.2)	197.9(27.6)	0.962(0.280)	1.69(0.499)
NGC4151	0.0081	1001.5(0.5)	137.5(1.1)	33.2(1.3)	71.2(0.7)	2.29(0.544)	0.312(0.026)
NGC4593	0.0075	2507.9(5.7)	378.9(11.5)	6.7(1.2)	243.8(8.1)	3.06(0.629)	8.32(0.782)
NGC5728	0.0090	2797.2(11.8)	409.4(23.7)	7.3(1.5)	217.0(13.6)	1.47(0.359)	4.08(0.598)
NGC5899	0.0071	2601.0(3.4)	495.4(6.7)	12.3(1.2)	235.8(3.4)	3.94(0.571)	6.14(0.476)
NGC5995	0.0096	7593.0(15.5)	438.8(31.0)	4.1(1.6)	...(...)	11.3(4.42)	...(...)
NGC6814	0.0088	1562.3(0.7)	88.5(1.5)	23.4(1.4)	72.8(1.9)	2.88(0.535)	0.358(0.035)
NGC7314	0.0094	1430.9(1.7)	317.3(3.4)	26.2(1.6)	152.5(1.8)	2.24(0.489)	1.47(0.123)
UGC12282	0.0087	5086.3(14.0)	682.1(28.1)	4.0(1.4)	319.5(13.8)	4.93(1.81)	19.0(2.23)

Note. — (1) Object Name. (2) RMS noise per channel calculated from background noise. (3) H I systemic velocity measured as the midpoint of the H I profile region defined by the 20% width. (4) 20% Width determined by the region of the H I profile that is above 20% of maximum peak value. (5) Integrated flux of the H I profile defined by the 20% width. (6) Maximum rotational velocity calculated using Equation 1. Due to unknown an inclination or an inclination of 0°, rotational velocity cannot be calculated. These objects have '...' listed in place of a result. (7) H I mass calculated using Equation 3. (8) Dynamical mass calculated using Equation 4. Again, some calculations were not possible due to unknown rotational velocity and were marked with '...' in place of a result.

3.3. Measurements

With the H I profiles in hand, we first measured the width at 20% of the peak value, called W_{20}. This will lead us to a measurement of the rotational velocity of the galaxy, but first, as outlined in Ho et al. (2008), some corrections must be made to W_{20}. The velocity resolution is 5 km s^{-1}, but increases by a factor of two from the Hanning smoothing to give us the instrumental correction of $W_{\rm inst}$ = 10 km s^{-1}. We must also correct for the impact of redshift on the observed line width, which is increased from the rest width by a factor of (1+z). Turbulent broadening caused by motions within the galaxy accounts for a slight increase in the observed line width. As in Ho et al. (2008), we will assume $W_{\rm turb} = 22$ km s^{-1}. Finally, we must correct for the inclination of the galaxy, where we assume the inclination of H I is the same as the optical inclination. The equation for the maximum rotational velocity considering all of these corrections is given by

$$v_m = \frac{(W_{20} - W_{inst})/(1+z) - W_{turb}}{2\sin i} \tag{1}$$

To find the inclination of each galaxy, we first found q, the ratio of optical minor-to-major axes listed in NED. We assume an intrinsic thickness of the disk of the galaxy, q_0, to be 0.3, which is the same assumption made in Ho et al. (2008). The formula relating the inclination to the axes ratio and the intrinsic thickness is

$$\cos^2 i = \frac{q^2 - q_0^2}{1 - q_0^2} \tag{2}$$

From the H I profile, we can also find the integrated line flux, $\int S_\nu d\nu$, in Jy km s^{-1}, which is the integrated flux contained in the 20% width. From Roberts (1962), we can relate integrated flux to H I mass by

$$M_{HI} = 2.36 \times 10^5 D_L^2 \int S_\nu d\nu M_\odot \tag{3}$$

From the RC3 catalog of de Vaucouleurs et al. (1991), we obtained D_{25}, the diameter at a surface level brightness of $\mu = 25$ mag arcsec^{-2}. D_{25} gives us an estimate of the galaxy's optical size. From Broeils & Rhee (1997) and Noordermeer et al. (2005), we estimate that the ratio of the diameter of the H I content compared to the diameter of the stellar content is ≈ 1.7. From Casertano & Shostak (1980), we can estimate the dynamical content using

$$M_{dyn} = 2 \times 10^4 \left(\frac{D_L}{\rm Mpc}\right) \left(\frac{D_{25}}{\rm arcmin}\right) \left(\frac{v_m}{\rm km * s^{-1}}\right)^2 M_\odot \tag{4}$$

The dynamical mass is largely made up of dark matter ($\sim 90\%$), so $M_{\rm dyn}$ gives us an estimate of the dark matter content of the galaxy (Rubin et al. 1980). Dark matter starts to take over the luminous mass within the dynamical mass between 5 to 10 kpc from the center of the galaxy (Rubin et al. 1980).

For objects with unknown inclinations, unknown optical diameters, or for face-on galaxies, the rotational velocities and dynamical masses could not be calculated. With face-on galaxies, we do not have any knowledge of how the galaxy is rotating because we do not see the blue- and red-shifted parts of the spiral disk. We therefore cannot determine the rotational velocities or dynamical masses of those objects. These derived quantities can be found in Table 4.

4. Analysis

4.1. H I Systemic Velocities

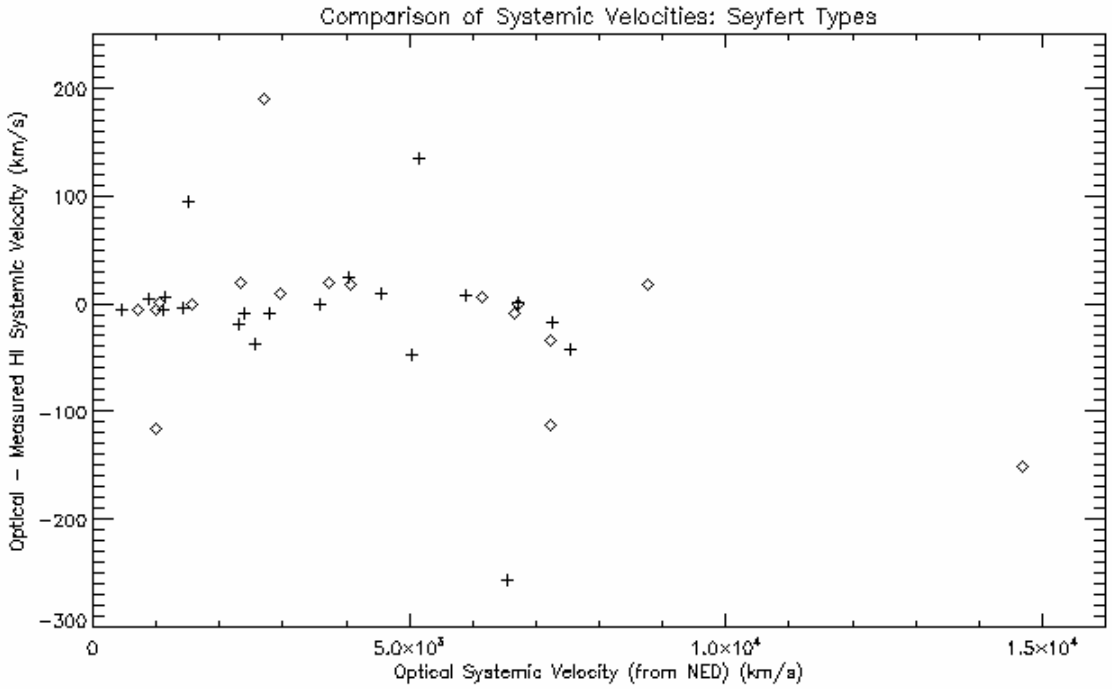

Fig. 5.— Comparison of H I systemic velocities to optical systemic velocities distinguished by Seyfert types. Diamonds indicate type I detections and plus signs are type II detections.

For most of the sources, the H I and optical systemic velocities fell within 50 km s^{-1} of one another, but there is a large spread from around −250 to +200 km s^{-1} (see Figure 5). This is similar to results found in Mirabel & Wilson (1984), Hutchings et al. (1987), and Ho et al. (2008). Our sample includes more Seyfert type II AGN than the other surveys, but it appears that type II do not behave distinguishably different than type I Seyferts as far as the differences in systemic velocities are concerned. Here we have used the convention of type I including 1, 1.2 and 1.5 Seyferts and type II including 1.8, 1.9, and 2 Seyferts. The most likely explanations for the disparity between the optical and H I systemic velocities stem from each of the data sets. The first explanation is from the H I emission. Though neutral hydrogen is usually considered to be a precise measurement tool, it can be misleading in interacting or disturbed galaxies. The H I content might not be uniformly distributed, which would cause the center of the H I profile to be different than the actual center of the galaxy. The other explanation is from the optical measurements. Our sample includes a population of obscured AGN, which do not exhibit as many optical lines. The measurement of the optical redshift will often rely on H II regions which are not found near the center of the galaxy where the AGN is located. Optical redshifts can also be affected by dust that reddens or obscures the emission. The optical measurements can also depend on where the NLR and BLR are located because they could be obscured by dust in the galaxy. Either data set could be the cause of the difference depending on each galaxy, but the disparity is unsurprising as it has been found in numerous other studies.

4.2. H I Mass

We will first examine the relationship between the cold gas content of the host galaxy and the accretion rate. As shown in Figure 6, the relationship between the accretion rate and the cold gas mass could be correlated. To find out, we calculated the correlation coefficient using

$$r = \frac{1}{N-1}\sum_{i=1}^{N}\left(\frac{X_i - X_{avg}}{s_X}\right)\left(\frac{Y_i - Y_{avg}}{s_Y}\right) \tag{5}$$

where N is the number of objects, $X_{\rm avg}$ is the average of the first data set, in this case it is log(X-ray luminosity), $Y_{\rm avg}$ is the average of the second data set, log(H I mass) in this case, and $s_{\rm X}$ and $s_{\rm Y}$ are the standard deviations of their respective data sets, given by

$$s_X = \sqrt{\frac{1}{N-1}\sum_{i=1}^{N}(X_i - X_{avg})^2} \tag{6}$$

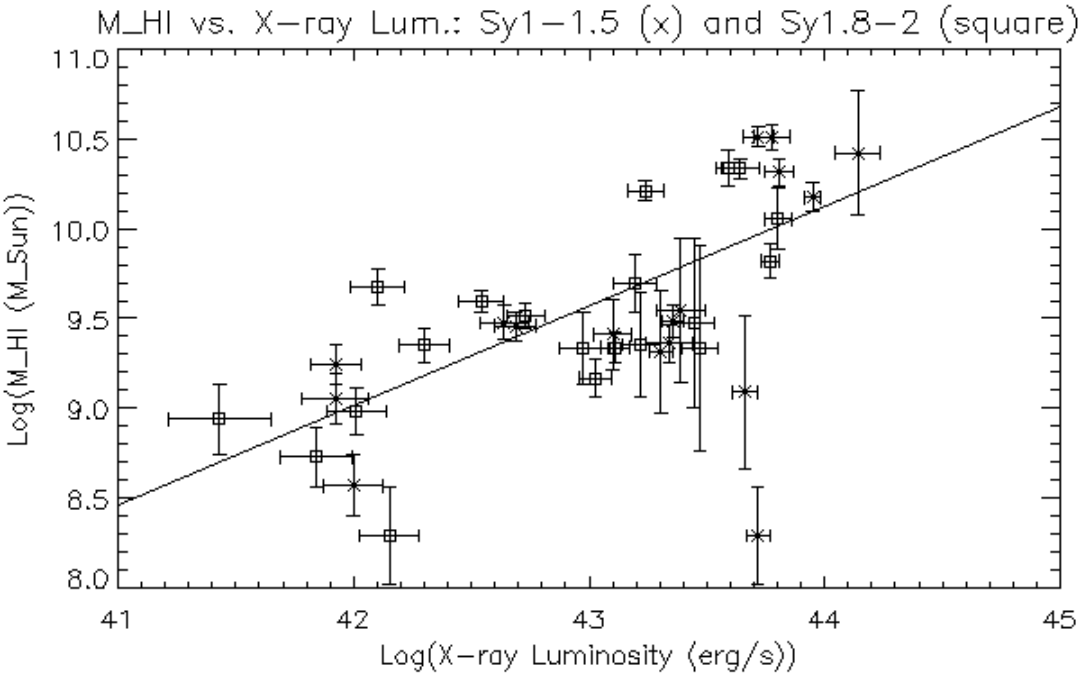

Fig. 6.— Neutral Hydrogen Mass vs. X-ray Luminosity. This graph shows the relationship between the accretion rate of the SMBH and the cold gas content of the galaxy with a fit described by Equation 8. This figure also distinguishes between Seyfert types (type I are Sy 1, 1.2, and 1.5; type II are Sy 1.8, 1.9, and 2).

The correlation coefficient gives us a measure of how well the two sets are related. A value of 1 corresponds to an absolute relation, -1 corresponds to an absolute inverse relation, and 0 corresponds to a scatter or non-relation. For this first relationship, the correlation coefficient is 0.621 for the 37 galaxies. To test the validity of the correlation coefficient, we must test the possibility of these sets begin uncorrelated. To do this, we perform a t-test, which is a test of the null hypothesis. The higher the t-value, the more unlikely it is that the sets are uncorrelated. The t-value is given by

$$t = \frac{r}{\sqrt{(1-r^2)/(N-2)}} \tag{7}$$

The resulting t-value for these two data sets is t=4.687. The probability corresponding to this t-value is <0.0001, which is beyond 4-sigma. This is the probability that the two sets are not correlated. Therefore we can confirm that the two data sets are correlated, meaning the accretion rate of the SMBH is related to the cold gas mass of the galaxy. In order to understand the relationship, we fit a line to the data using a linear least squares regression

(see Figure 6). The resulting fit is

$$Log\left(\frac{M_{HI}}{\mathrm{M}_{\odot}}\right) = 0.55 \times Log\left(\frac{L_{X-ray}}{\mathrm{erg} * \mathrm{s}^{-1}}\right) - 14.23 \tag{8}$$

To further understand this relationship, we search for any difference between the cold gas content of hosts with unobscured and obscured AGN. As shown in Figure 6, both type I and type II Seyferts are spread throughout the graph. There is no distinguishing property of the cold gas content in the hosts of these two types of AGN.

To check this correlation and fit, we now omit the objects with low signal-to-noise (see Figure 3), leaving only the objects with higher signal-to-noise to use in the correlation and fit (see Figure 7). For the 28 objects with higher signal-to-noise ratios, the new correlation coefficient is 0.658, with a t-value of 4.456 and a corresponding probability of <0.0001. The new fit for these objects is

$$Log\left(\frac{M_{HI}}{\mathrm{M}_{\odot}}\right) = 0.56 \times Log\left(\frac{L_{X-ray}}{\mathrm{erg} * \mathrm{s}^{-1}}\right) - 14.26 \tag{9}$$

We see that by removing these unreliable objects, our fit slightly improves and the correlation holds.

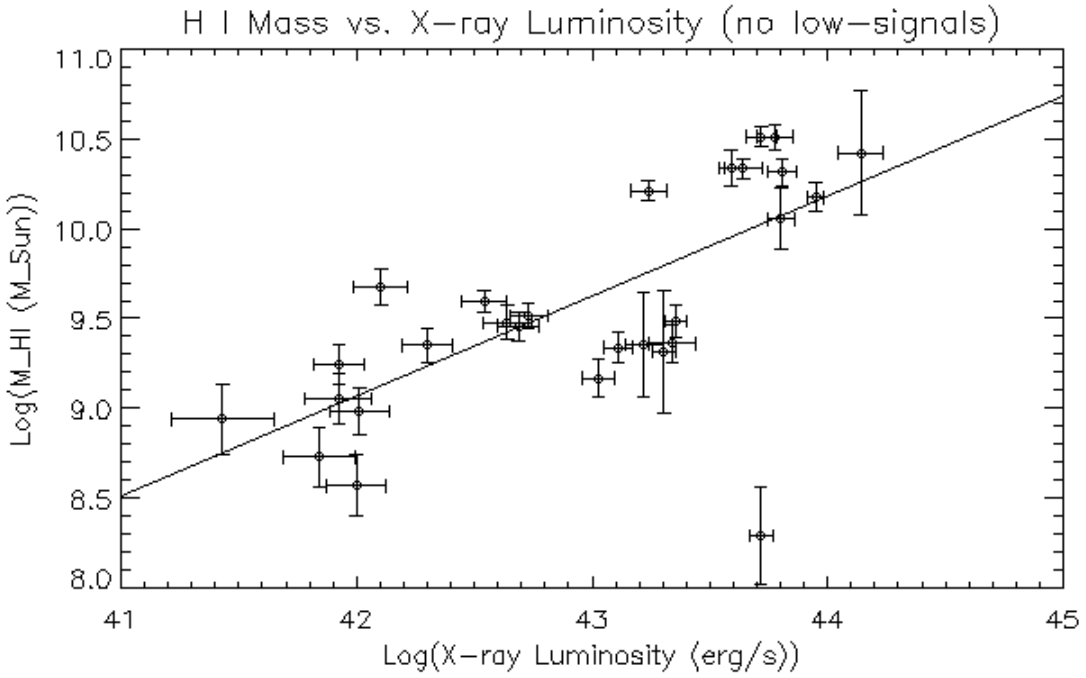

Fig. 7.— Neutral Hydrogen Mass vs. X-ray Luminosity (without low signal-to-noise objects). This graph shows the relationship between the accretion rate of the SMBH and the cold gas content of the galaxy with a fit described by Equation 9.

4.3. Dynamical Mass

The relationship between the X-ray luminosity and the dynamical mass does not immediately appear as correlated (see Figure 8). Here, we also perform a correlation coefficient calculation and t-test for these two data sets. The correlation coefficient here is 0.555 for the 27 galaxies. The corresponding t-value is 3.336 with a probability of 0.0013 (3-sigma) that the two sets are uncorrelated. This is a small probability, which means that the two data sets are correlated. Consequently, the accretion rate of the SMBH is related to the dynamical mass of the galaxy and thus related to the dark matter mass of the galaxy. This relationship can be described by the following equation found from a least squares fit (see Figure 8).

$$Log\left(\frac{M_{dyn}}{\mathrm{M}_{\odot}}\right) = 0.44 \times Log\left(\frac{L_{X-ray}}{\mathrm{erg} * \mathrm{s}^{-1}}\right) - 8.04 \tag{10}$$

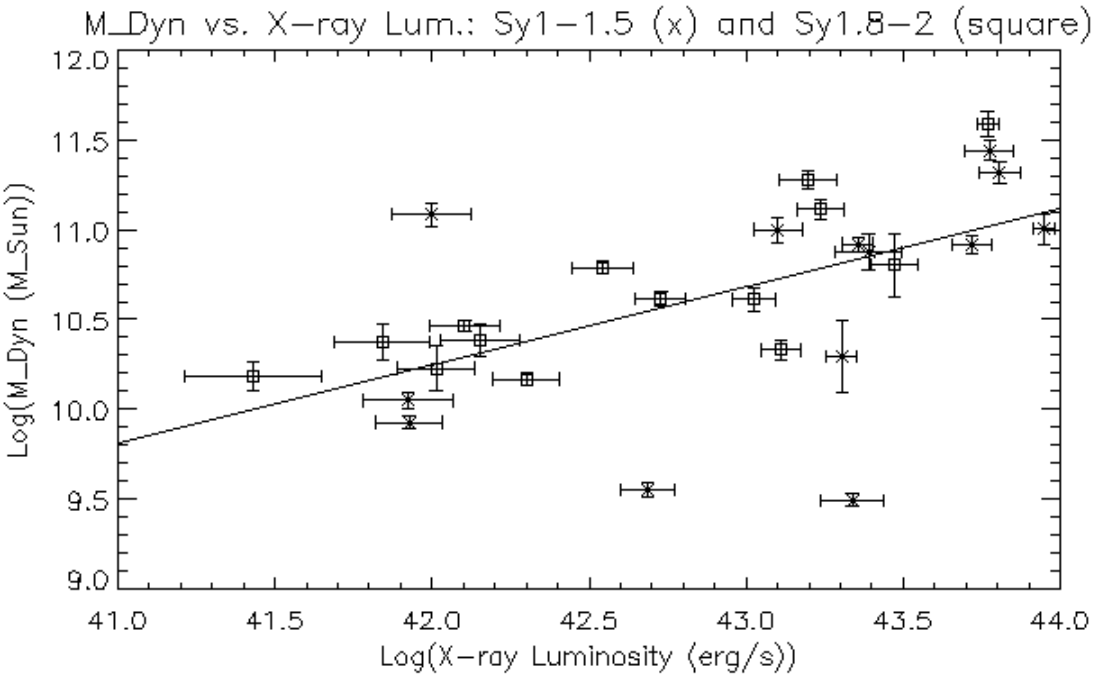

Fig. 8.— Dynamical Mass vs. X-ray Luminosity. This graph shows the relationship between the accretion rate of the SMBH and the dark matter content of the galaxy with a fit line described by Equation 10. This graph also distinguishes between Seyfert types (type I are Sy 1, 1.2, and 1.5; type II are Sy 1.8, 1.9, and 2).

For this relationship, we will also look for any distinguishing features based on Seyfert types (see Figure 8). Again, there do not seem to be any discernible differences between the dark matter content (dynamical mass) of host galaxies with obscured and unobscured AGN. The ranges of the dark matter content for obscured and unobscured AGN are too similar to contrast in any definite way.

We again remove objects with low signal-to-noise ratios (see Figure 9). The resulting correlation coefficient is 0.480 for 21 sources. The corresponding t-value is 2.385 with a probability of 0.014 (2.2-sigma). Removing the low signal-to-noise objects has lowered the probability that these sets are correlated, but the probability from the t-test (the probability for non-correlation) is still below the threshold probability value of 0.05. The new fit line for this data set is

$$Log\left(\frac{M_{dyn}}{\mathrm{M}_{\odot}}\right) = 0.43 \times Log\left(\frac{L_{X-ray}}{\mathrm{erg} * \mathrm{s}^{-1}}\right) - 7.92 \tag{11}$$

4.4. Comparison to Literature

To augment our sample, we added Seyfert galaxies observed by Ho et al. (2008) that were also observed in the Swift BAT 70-month survey (Baumgartner et al. 2012). From this study, we have gathered measurements of the H I mass, rotational velocity, and dynamical mass for 22 additional galaxies, described in Table 6. Additionally, 7 of our galaxies were observed in their study (see Table 5), allowing us to compare our results. All but one of the 22 additional galaxies is either a Seyfert 1, 1.2, or 1.5. Because there is no noticeable difference between type I and type II Seyferts in terms of their H I masses and dynamical masses, augmenting our sample with this additional data should not cause much of a bias in the results.

Comparing the common emissions between our study and that of Ho et al. (2008), we see the largest discrepancies between the data sets are the optical diameter, D_{25}, and the maximum rotational velocity, v_{m} (see Table 5). These differences cause the disparity between the two dynamical masses (see Equation 4). It is odd that there are significant differences in the maximum rotation velocities. We used the same assumptions and corrections in our calculations as were made in Ho et al. (2008). This means the difference comes from either the inclination or the 20% width. The difference is most likely due to the inclination. Neutral hydrogen transitions happen so rarely, it is highly unlikely for us to observe two different

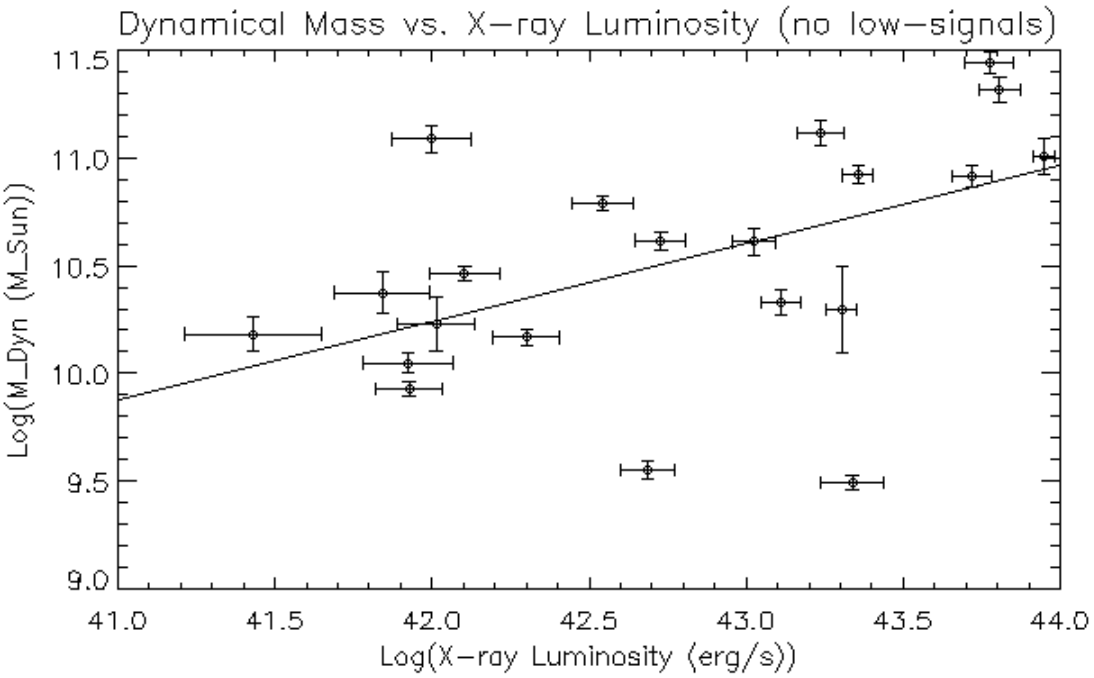

Fig. 9.— Dynamical Mass vs. X-ray Luminosity (without low signal-to-noise objects). This graph shows the relationship between the accretion rate of the SMBH and the dark matter content of the galaxy with a fit line described by Equation 10. This graph also distinguishes between Seyfert types (type I are Sy 1, 1.2, and 1.5; type II are Sy 1.8, 1.9, and 2).

amounts of H I. This is justified by the fairly similar results of the H I masses. Therefore, the inclination measurements must be the cause of the difference in maximum rotational velocities calculated for each galaxy.

Adding these new sources to our sample, we can test the relationships we found in Sections 4.2 and 4.3. First, the new correlation coefficient for the relation between X-ray luminosity and H I mass for our sample with the addition of the Ho et al. (2008) galaxies is 0.4691 for 59 total galaxies. This results in a t-value of 4.01 and a probability of <0.0001 (beyond 4-sigma) that the data sets are uncorrelated. This confirms our initial conclusion that accretion rate (X-ray luminosity) of the SMBH is related to the H I mass of the host galaxy. The new parameters of this relationship (see Figure 10) are given in the following equation

$$Log\left(\frac{M_{HI}}{\mathrm{M}_{\odot}}\right) = 0.37 \times Log\left(\frac{L_{X-ray}}{\mathrm{erg} * \mathrm{s}^{-1}}\right) - 6.46 \tag{12}$$

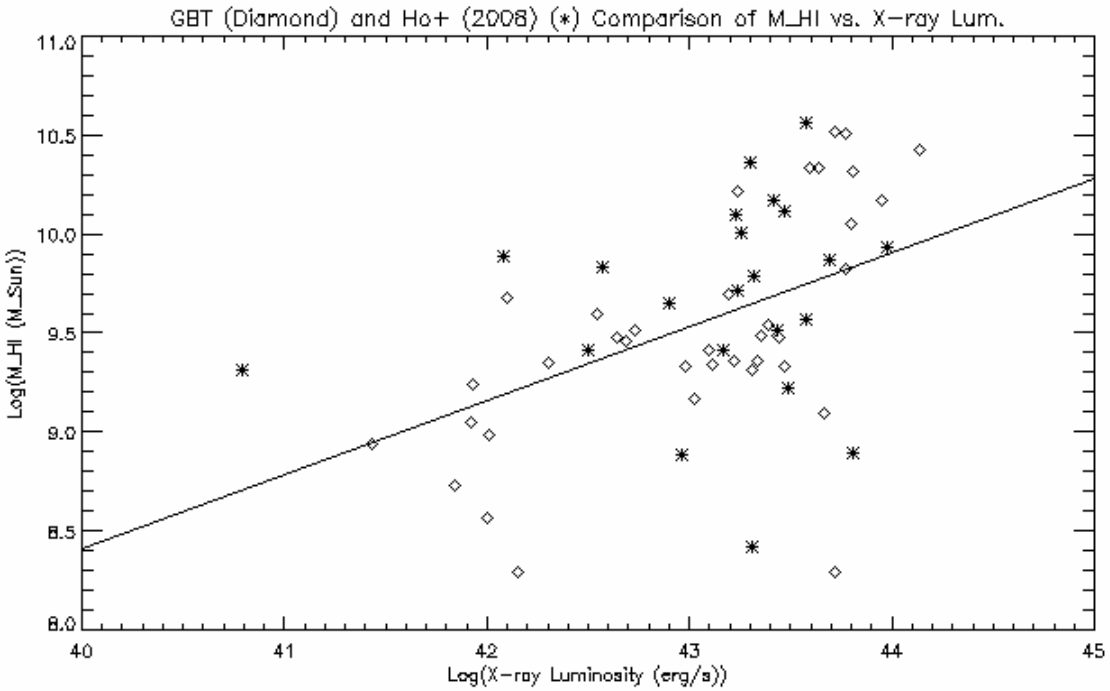

Fig. 10.— H I Mass vs. X-ray Luminosity. This graph shows the relationship between the accretion rate of the SMBH and the cold gas mass of the galaxy for the expanded data set, which includes the low signal-to-noise ratio objects we previously removed.

Table 5. Comparison to Ho et al. (2008) Data: Columns (a) = Our Data, Columns (b) = Ho et al. (2008) Data

Object Name (1)	$D_{\rm L}$ (Mpc) (2a)	$D_{\rm L}$ (Mpc) (2b)	D_{25} (arcmin) (3a)	D_{25} (arcmin) (3b)	$v_{\rm m}$ (km s^{-1}) (4a)	$v_{\rm m}$ (km s^{-1}) (4b)	Log($M_{\rm H\ I}$) (log(M$_\odot$)) (5a)	Log($M_{\rm H\ I}$) (log(M$_\odot$)) (5b)	Log($M_{\rm dyn}$) (log(M$_\odot$)) (6a)	Log($M_{\rm dyn}$) (log(M$_\odot$)) (6b)	Log($L_{\rm X\text{-}ray}$) (log(erg s^{-1})) (7a)	Log($L_{\rm X\text{-}ray}$) (log(erg s^{-1})) (7b)
ESO362-18	52.1	53.7	1.08	1.29	132.3	125.5	9.31	9.31	10.29	10.34	43.31	43.23
MCG+08-11-011	87.9	88.0	1.32	2.75	208.2	312.0	10.17	10.18	11.00	11.67	43.95	44.10
Mrk10	126.4	126.6	1.25	1.51	295.6	255.7	10.51	10.68	11.44	11.40	43.78	43.46
NGC4051	12.7	9.7	1.72	5.13	160.5	209.9	9.05	9.15	10.05	10.64	41.92	41.67
NGC4151	17.1	14.0	1.80	3.80	71.2	144.6	9.36	9.46	9.49	10.35	43.34	43.12
NGC4593	44.0	38.3	1.59	2.63	243.8	274.6	9.49	9.37	10.92	11.18	43.36	43.20
NGC6814	22.8	22.0	1.48	3.55	72.8	98.2	9.46	9.60	9.55	10.18	42.69	42.67

Note. — (1) Object Name. (2a) Luminosity distance in our sample. (2b) Luminosity distance in Ho et al. (2008). (3a) Optical diameter from our sample, found in the RC3 Catalog of de Vaucouleurs et al. (1991). (3b) Optical diameter from Ho et al. (2008). (4a) Maximum rotational velocity from our sample. (4b) Maximum rotational velocity from Ho et at. (2008). (5a) Log(H I mass) from our sample. (5b) Log(H I mass) from Ho et al. (2008). (6a) Log(Dynamical mass) from our sample. (6b) Log(Dynamical mass) from Ho et al. (2008). (7a) Log(X-ray Luminosity) from our sample. (7b) Log(X-ray Luminosity) from the Swift BAT 70-month survey.

Table 6. Ho et al. (2008) Data

Object Name (1)	Seyfert Type (2)	$D_{\rm L}$ (Mpc) (3)	D_{25} (arcmin) (4)	$v_{\rm m}$ (km s^{-1}) (5)	Log($M_{\rm H\ I}$) (log($M_\odot$)) (6)	Log($M_{\rm dyn}$) (log($M_\odot$)) (7)	Log($L_{\rm X\text{-}ray}$) (log(erg s^{-1})) (8)
NGC7811	1.5	109.8	0.41	255.2	9.71	10.77	43.24
MCG+05-03-013	1	155.9	1.02	263.4	10.12	11.34	43.47
Mrk352	1	63.7	0.68	182.9	9.41	10.46	43.17
Mrk975	1	217.6	0.98	223.9	9.93	11.35	43.98
Mrk359	1.5	74.5	0.78	38.0	8.88	9.22	42.96
Mrk590	1.2	113.8	1.23	372.3	10.17	11.59	43.42
NGC931	1.5	71.4	2.95	208.3	10.56	11.26	43.58
Mrk1044	1	70.6	0.83	171.8	9.65	10.54	42.90
NGC1566	1	21.2	8.13	117.2	9.89	10.68	42.08
UGC03142	1	93.2	1.86	208.9	9.87	11.18	43.69
UGC03478	1.2	54.6	1.23	169.9	9.83	10.59	42.57
Mrk704	1.5	126.1	0.78	133.0	8.89	10.54	43.81
Mrk705	1.2	126.1	0.71	198.4	9.22	10.85	43.49
NGC3080	1	153.6	0.83	226.2	10.10	11.12	43.23
NGC3516	1.5	37.4	2.04	296.0	8.42	11.13	43.31
ARP151	1	90.6	0.81	100.0	10.36	10.17	43.30
Mrk739E	1	129.2	0.62	234.9	9.51	10.95	43.43
NGC3783	1	41.3	2.29	125.7	9.57	10.48	43.58
NGC4395	1.9	4.6	4.07	84.0	9.31	9.42	40.79
Fairall 51	1	60.6	2.09	130.3	10.01	10.63	43.26
NGC7214	1.2	99.3	2.00	210.7	9.79	11.25	43.32
NGC7213	1.5	24.6	3.80	378.6	9.41	11.43	42.50

Note. — (1) Object Name. (2) Seyfert type from Swift BAT 70-month survey. (3) Luminosity distance. (4) Optical diameter from Ho et al. (2008). (5) Maximum rotational velocity from Ho et al. (2008). (6) Log(H I mass) from Ho et al. (2008). (7) Log(Dynamical mass) calculated from columns 3, 4, and 5 using Equation 4. (8) Log(X-ray Luminosity) taken directly from Swift BAT 70-month survey.

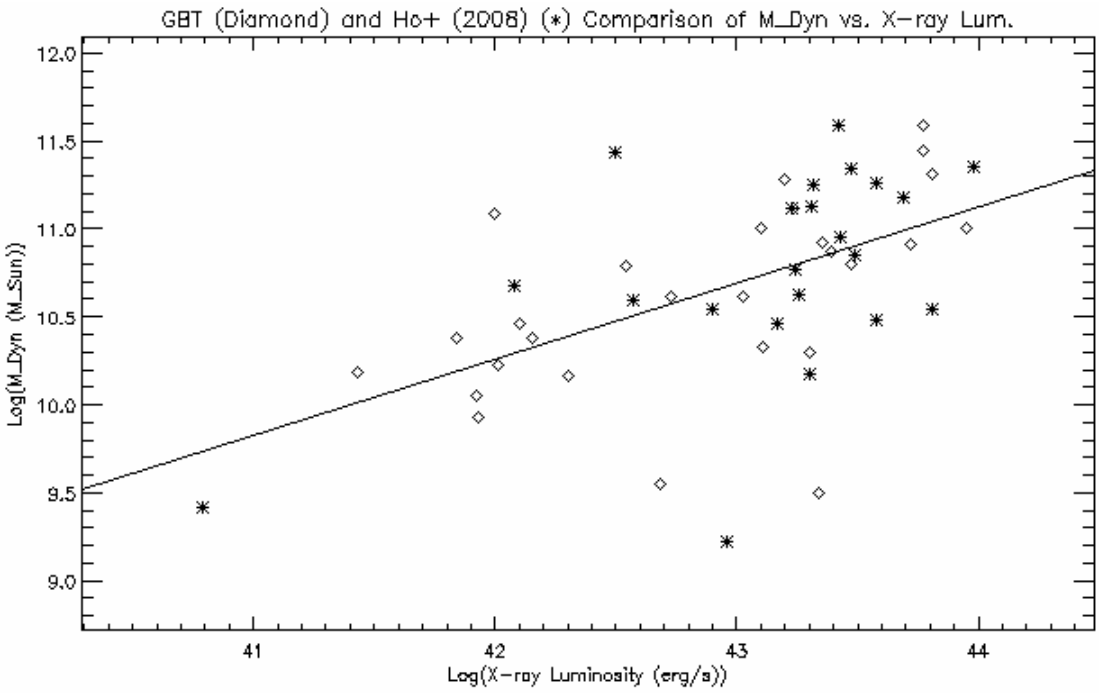

Fig. 11.— Dynamical Mass vs. X-ray Luminosity. This graph shows the relationship between the accretion rate of the SMBH and the dark matter content of the galaxy.

We also tested the relationship between X-ray luminosity of the AGN and dynamical mass of the host galaxy. The new correlation coefficient for our sample with those from Ho et al. (2008) is 0.547 for 49 galaxies. The t-value for this coefficient is 4.48 with a probability of <0.0001 that the two sets are uncorrelated. This gives us a relationship between the accretion rate of the SMBH and the dark matter content of the host galaxy. This relationship (see Figure 11) takes the form of

$$Log\left(\frac{M_{dyn}}{\mathrm{M}_{\odot}}\right) = 0.43 \times Log\left(\frac{L_{X-ray}}{\mathrm{erg} * \mathrm{s}^{-1}}\right) - 7.92 \tag{13}$$

5. Discussion

Although we did not predict relationships between the accretion rate of the SMBH and the cold gas content or dark matter mass of the host (see Section 1.3), we have found strong evidence of a connection. The relationship between the cold gas mass of the host and the accretion rate of the AGN (see Section 4.2) is very unusual. Previous work has linked gas

content to the AGN have been at small radii (r < 1 kpc), but neutral hydrogen is distributed much further out in the host galaxy (Broeils & Rhee 1997). Due to the distance of most of the H I gas, we would expect the AGN to have no connection to the global H I mass. Instead of accreting according to the mass of nearby gas, the SMBH is accreting with relation to the entire host. Our results are also in stark contrast to the results of Ho et al. (2003), where they found the optical accretion rate not to be correlated to the H I mass of the host. Their optical accretion was derived from the Hα line, a broad line in AGN spectra. The hard X-ray emission is solely from the accretion disk in the AGN, but the exact origin of this emission is not understood. Many models suggest the X-rays are produced through inverse-Compton scattering of high-energy electrons with lower-energy photons. Some of those models assert that they are produced by optical and ultraviolet photons that are boosted in energy by inverse-Compton scattering off relativistic electrons. If this is indeed the case, the number of ultraviolet and optical photons should be proportional to the number of X-ray photons. Thus, the luminosities from the two spectral regions should be related in some way. Our findings and those of Ho et al. (2003) suggest opposing conclusions. The difference in our results must come from the the accretion rate. As discussed in Section 1.1, Seyfert types are determined by optical spectra. With varying Seyfert types come varying strengths of Hα. Interstellar gas and dust can block some optical emission and thus throw off the optical measurements. Our choice to use the hard X-ray emission largely removes this problem. This could be an explanation as to the disparity between our results and those of Ho et al. (2003). However, more work must be done to confirm the correct result.

We suggest the AGN is related to the cold gas mass in the rest of the galaxy. Based on this conclusion, it is easier to understand the correlation between the dark matter mass and the X-ray accretion rate of the SMBH (see Section 4.3). Ho et al. (2008b) found a relationship between the SMBH mass and the dynamical mass of the host. We have found a similar relationship to the dynamical mass, except we are considering the accretion instead of the mass of the SMBH. The SMBH is correlated with the dark matter content of its host and is accreting in a similar fashion. This is also an unusual result because the dynamical mass only starts do be dominated by dark matter at larger radii (r > 5 kpc). Here, again, we see that the SMBH "knows" about mass contents of the host much further out in the galaxy. Dark matter mainly resides in the halo of the galaxy, far away from the central AGN region. Dark matter does not interact with light and has never been directly observed, only inferred through its gravitational effects. If the accretion of the SMBH is related to the amount of dark matter in the host galaxy, this may indicate that the relationship stems from gravitational effects of the dark matter with the SMBH. Again, this result must be checked through new studies in order for our conclusion to be confirmed.

The correlations we have found are new; no study of this nature has yet been completed, so our results remain unconfirmed by the literature. However, we can take steps to check our results. We must add published optical data (from Koss 2011 and other sources) that will give us the masses of the SMBHs for all of our objects. We can then examine how significant our accretion rates are by looking at the fractional accretion of each SMBH (how much the SMBH is accreting with respect to how massive the SMBH is). From there, we can compare the cold gas and dark matter content with the fractional accretion rate of the SMBH for each galaxy. This would indicate if the correlation is true or just an effect of having larger phenomena in more massive galaxies.

6. Conclusion

We have used the GBT to conduct a unique survey of Seyfert galaxies selected from the Swift BAT 22-month survey. The sample consists of 95 nearby galaxies at redshifts below 0.05, or within 220 Mpc. Optical data were found using NED. Out of the 95 galaxies in our study, we observed 37 emission detections, 4 absorption detections, 2 galaxies with prominent continua, and 6 galaxies that remain unclassified due to solar interference. For the emission detections, we derived the H I mass and dynamical mass of the galaxies. We used the Swift BAT 22-month survey to find the X-ray luminosity of the AGN giving us a measure of the accretion rate of the SMBH. We found significant evidence of a correlation between the accretion rate of the SMBH and the cold gas mass of the host galaxy and a correlation between the accretion rate of the SMBH and the dark matter mass of the host galaxy. We presented the parameters of the relationships as well as a comparison of our findings with results from the literature.

This work was supported by NRAO student funds from the project GBT12A-253 as well as student funds from the Center for Astrophysics and Space Astronomy at the University of Colorado, Boulder. This research has made use of the NASA/IPAC Extragalactic Database (NED) which is operated by the Jet Propulsion Laboratory, California Institute of Technology under contract with the National Aeronautics and Space Administration (http://ned.ipac.caltech.edu).

REFERENCES

Baumgartner, W. H., Tueller, J., Markwardt, C. B., Skinner, G. K., Barthelmy, S., Mushotzky, R. F., Evans, P., & Gehrels, N. 2012, ApJS, 207, 19

Broeils, A. H., & Rhee, M.-H. 1997, A&A, 324, 877

Casertano, S. P. R., & Shostak, G. S. 1980, A&A, 81, 371

Diamond-Stanic, A. M. & Rieke, G. H. 2012, 746, 168

Esquej, P., Alonso-Herrero, A., González-Martín, O., Hönig, S. F., Hernán-Caballero, A., Roche, P., Ramos Almeida, C., Mason, R. E., Díaz-Santos, T., Levenson, N. A., Aretxaga, I., Rodríguez Espinosa, J. M., & Packham, C. 2014, ApJ, 780, 86

Heckman, T. M., Balick, B., & Sullivan, W. T. 1978, ApJ, 224, 745

Ho, L. C., Darling, J., & Greene, J. E. 2008, ApJS, 177, 103

Ho, L. C., Darling, J., & Greene, J. E. 2008b, ApJ, 681, 128

Ho, L. C., Filippenko, A. V., & Sargent, W. L. W. 2003, ApJ, 583, 159

Hutchings, J. B., Gower, A. C., & Price, R. 1987, AJ, 93, 6

Koss, M., Mushotzky, R., Veilleux, S., Winter, L. M., Baumgartner, W., Tueller, J., Gehrels, N., & Valencic, L. 2011, ApJ, 39, 57

Mirabel, I. F., & Wilson, A. S. 1984, ApJ, 277, 92

Noordermeer, E., van der Hulst, J. M., Sancisi, R., Swaters, R. A., & van Albada, T. S. 2005, A&A, 442, 137

Roberts, M. S. 1962, AJ, 67, 437

Rubin, V. C., Ford, W. K. Jr., Thonnard, N. 1980, ApJ, 238, 471

Tueller, J., Baumgartner, W. H., Markwardt, C. B., Skinner, G. K., Mushotzky, R. F., Ajello, M., Barthelmy, S., Beardmore, A., Brandt, W. N., Burrows, D., Chincarini, G., Campana, S., Cummings, J., Cusumano, G., Evans, P., Fenimore, E., Gehrels, N., Godet, O., Grupe, D., Holland, S., Kennea, J., Krimm, H. A., Koss, M., Moretti, A., Mukai, K., Osborne, J. P., Okajima, T., Pagani, C., Page, K., Palmer, D., Parsons, A., Schneider, D. P., Sakamoto, T., Sambruna, R., Sato, G., Stamatikos, M., Stroh, M., Ukwata, T., & Winter, L. M. 2010, ApJS, 186, 378

de Vaucouleurs, G., de Vaucouleurs, A., Corwin, H. G., Buta, R. J., Paturel, G., Fouque, P. 1991, Springer-Verlag

---

This preprint was prepared with the AAS LaTeX macros v5.2.